

Large-field-of-view, modular, stabilized, adaptive-optics-based scanning laser ophthalmoscope

Stephen A. Burns

School of Optometry, Indiana University, Bloomington, Indiana 47405, USA

Remy Tumbar

Cornell University, Ithaca, New York 14853, USA

Ann E. Elsner

School of Optometry, Indiana University, Bloomington, Indiana 47405, USA

Daniel Ferguson and Daniel X. Hammer

Physical Sciences Inc., Andover, Massachusetts 01810-1077, USA

Received September 6, 2006; accepted October 30, 2006;
posted October 30, 2006 (Doc. ID 74768); published April 11, 2007

We describe the design and performance of an adaptive optics retinal imager that is optimized for use during dynamic correction for eye movements. The system incorporates a retinal tracker and stabilizer, a wide-field line scan scanning laser ophthalmoscope (SLO), and a high-resolution microelectromechanical-systems-based adaptive optics SLO. The detection system incorporates selection and positioning of confocal apertures, allowing measurement of images arising from different portions of the double pass retinal point-spread function (psf). System performance was excellent. The adaptive optics increased the brightness and contrast for small confocal apertures by more than $2\times$ and decreased the brightness of images obtained with displaced apertures, confirming the ability of the adaptive optics system to improve the psf. The retinal image was stabilized to within $18\mu\text{m}$ 90% of the time. Stabilization was sufficient for cross-correlation techniques to automatically align the images. © 2007 Optical Society of America

OCIS codes: 170.1790, 170.3890, 170.4460, 330.2210, 330.4300, 010.1080.

1. INTRODUCTION

Correction of wavefront aberrations introduced by the human eye by using adaptive optics (AO) has been shown to provide superior resolution and contrast in retinal imaging.^{1–6} Systems using wavefront corrections include flood illuminated systems,^{1,2} AO scanning laser ophthalmoscopes (AOSLOs),^{5–9} and AO optical coherence tomography (AOCT),^{10–13} as well as multifunctional systems.¹⁴ While flood illuminated systems have been shown to provide excellent imaging performance, they do not control for depth of field and stray or scattered light essential to high-contrast imaging and intrinsic depth sectioning capability. AOSLO and AOCT instrumentation address these limitations by using techniques that make them sensitive to only a narrow depth of field or to primarily singly scattered light with high axial resolution low-coherence techniques.

In clinical disease, one of the strongest signs is often increased retinal scattering due to changes in tissue properties.^{15–21} Most AO systems typically operate at high resolution and have a restricted field of view (FOV) (1 to

3 deg), making it difficult to identify the exact retinal locus of the high-resolution view in relation to clinically observed changes. It becomes even more difficult to understand images that include structures never visualized before *in vivo*, since the surrounding and more familiar retinal structures are not within the FOV. One approach to alleviate this problem is to construct a montage of small-field retinal images with known spatial relations to one another. This is a relatively straightforward solution for individuals with good fixation and can be accomplished by systematically moving a fixation target and performing *post hoc* image alignment in a series. However, it is more difficult in individuals who do not fixate accurately, since entire portions of the retina may be skipped unintentionally. Finally, in the case of AOSLO and AOCT imaging, which build up raster images sequentially, eye movements can cause shearing of the retinal image within a frame and poor registration between frames. While software algorithms²² can help with this, it is not yet clear over what range of retinal motion velocities and saccadic amplitudes they can operate.

In this paper we describe the design and implementation of a tracking AOSLO designed to overcome some of the above limitations. We incorporated a configurable detection channel^{23–25} to allow rapid changes in the imaging mode, from tightly confocal, which provides a narrow depth of field^{26–28} dominated by directly backscattered light, to large-aperture scanning, which incorporates light from both the peak and tails of the double pass point-spread function (psf), as well as several stages in between.^{15,24,29} In addition, the confocal aperture position is under computer control, allowing assessment of the information coming back from different portions of the psf. To provide both a context for the high-resolution image, as well as to correct for most eye movements in real time, we have incorporated a real time tracking system^{7,30–32} that provides both a wide-field view of the retina using a line-scanning laser ophthalmoscope (LSLO) and a real time retinal tracker. The tracking system stabilizes the AO raster on a desired retinal region, but with a simple sequence of offsets it also provides the ability to construct a retinal montage by rapidly adding offsets to the tracking galvanometers. This ability to move the high-resolution AO field within the FOV of the system without changing fixation allows rapid construction of a larger view, but it creates the constraint that the field aberrations of the optical system be small. By performing the montage scanning and descanning at the pupil plane closest to the eye, we ensured that most of the optical train effectively sees only the zero-field position. This decreases system aberrations and allows a diffraction limited system over the entire range of scan angles using off-the-shelf components.

Finally, because a goal of this system is to image a wide variety of retinal conditions, we incorporate a supplementary focusing system that allows us to move our plane of focus through the retinal layers dynamically without using the limited focusing range of the microelectromechanical systems (MEMS) mirror. In older subjects or those with high aberrations, this allows us to compensate the large aberrations present in older eyes³³ using the deformable mirror and to change the focal plane using the supplementary system. Just as it was desirable to place most of the scanning elements close to the eye, it was desirable to place the focusing system close to the eye, allowing most of the optical system to work with an in-focus image. As a result, most of the optical system works at high f -number, decreasing both focus-dependent aberrations and other optical problems such as vignetting. The system we describe has some features in common with a system described previously⁷ in that it includes similar technology for tracking and stabilization, but there are several major differences, in particular the design of the SLO as noted and the detection channel, as well as the interface between optical subsystems.

2. METHODS

The system is composed of four primary optical subsystems, the AOSLO scanner, the wavefront sensor (WFS), the configurable detection system, and the wide-field tracking–stabilization system. There are separate control computers for the wavefront sensing and correcting and for the eyetracking and image stabilization.

These systems are in turn controlled by the retinal imaging computer, which has direct control of the focus and detection channel as well.

A. AOSLO Optical Design

There were several optical design goals for our system. First, we planned to use a Boston Micromachines MEMS mirror because of its compact size, ability to work over a wide range of aberrations (each actuator has a limited influence on adjacent apertures), and relatively good surface quality. However, this MEMS mirror has only a 4 μm stroke, and thus it can correct only up to 8 μm of optical path difference. Thus, we require additional forms of correction for lower-order aberrations.³⁴ Defocus is varied in an SLO system for two purposes: first, to correct for the ametropia state of a subject's eye and second, to allow the operator to choose the depth in the retina at which the AOSLO is focused. The retina is not a flat surface, and even in otherwise healthy eyes there are significant differences between the foveal pit and the surrounding retina, as well as from the elevated neuroretinal rim to the lamina cribrosa in the cup. While in principle this second type of focusing could be done with the MEMS mirror, this is dependent on the degree to which the stroke of the MEMS is used in correcting high-order aberrations. Eye tracking and building up a wide-field view add additional constraints in that the system must be able to provide a near-diffraction-limited view of the retina over a relatively large range of angles (because the beam may be displaced 5 deg during a small saccade). Thus we designed the AOSLO to provide diffraction limited performance over a $\pm 10^\circ$ FOV. The solution for obtaining this combination of requirements was to use a combination of excellent optics for the design, to incorporate a dynamic computer-controlled focusing system, and to leave a provision for inserting correcting lenses.

Figure 1 is an optical schematic of the resulting optical system. The imaging beam (SLD1) is provided by a Superlum Broadlighter light source, with a 50 nm bandwidth centered at 840 nm. This SLD is coupled into the imaging system using a wedged beam splitter (BS1). Light from the SLD is relayed onto the deformable mirror (DM) by the first pair of relay mirrors (SM1, SM2). Light from the DM is relayed onto the fast scanner FS (an 8 kHz resonant scanner from EOPC) by turning mirrors and another pair of relay mirrors (SM3, SM4), which provide rapid horizontal scanning. The horizontal scanner is then relayed onto a slow, vertical-scan galvanometer (VS) using a pair of mirrors (SM5, SM6), which are off axis vertically (Fig. 1, inset). Just after VS (between the eye and the VS), a pair of galvanometers are located (SG1 and SG2—not shown because they are vertically placed), which steer the beam under the control of the tracking system. These mirrors are used in the tracking system to control the location of the retinal field being imaged (see below). That is, the VS mirror deflects the beam onto a vertical steering mirror and then onto a horizontal steering mirror. These two additional galvanometers are placed such that they approximately bracket an optical conjugate to the center of rotation of the eye, and when driven by the tracking system, they allow for compensation of eye movements and move the pupil of the system to compensate rotation

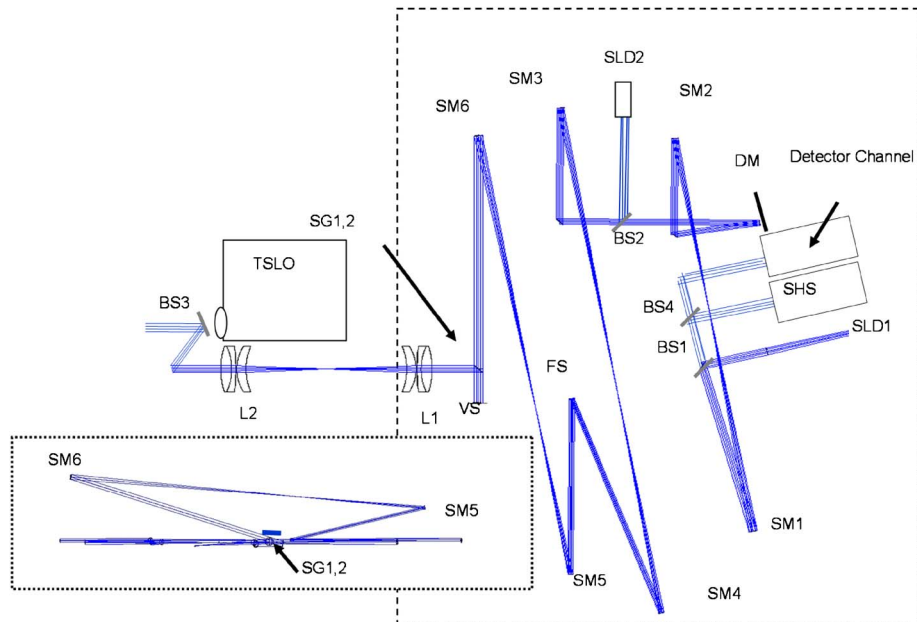


Fig. 1. (Color online) Schematic of the optical layout of the AOSLO. Details are provided in the text. Inset: To compensate for the cumulative astigmatism from the off-axis relay mirrors, the final pair of mirrors (SM6, SM7) are offset vertically, adding vertical astigmatism, which cancels the horizontal astigmatism from the rest of the system.

induced changes in pupil position, as well as tracking the retinal location.³¹ Finally, the scanned beam is relayed into the eye using a pair of relay lenses (L1, L2). Because the optical design for the wide-field system³¹ (see below) requires very different trade-offs than for a high-resolution small-field system, we kept the two optical systems as independent as possible, and thus we use a dichroic beam splitter (BS3) to combine light from the wide-field/tracking system (>900 nm) with the imaging system (<900 nm).

To provide a diffraction limited design for mounting and tracking the high-resolution imaging field over a range of positions, we placed the deflectors for the scanning and tracking system, as well as the focusing system, close to the eye to maintain as low a numerical aperture as possible for the optical field propagating through the optical train for as much of the system path as possible. Because it has a relatively small stroke, the MEMS mirror, generates relatively smaller angles of incidence in our system than in the Badal or scanning systems. We therefore placed the MEMS mirror farther from the eye, minimizing the angles of incidence on mirrors SM1–SM4.

Even with the small angles at the spherical mirrors, off-axis astigmatism accumulates in the system. To compensate for this off-axis astigmatism, we folded the final pair of mirror relays (from the fast-scan resonant galvanometer to the slow-scan galvanometer) out of the plane of the rest of the optical system (Fig. 1, inset).²⁵ The angle that minimizes system astigmatism was calculated using Zemax. Our optimization resulted in a diffraction limited performance over at least the 3 deg FOV that can be produced by the fast scanner (FS). The design has an RMS wavefront error under $\lambda/20$ and a Strehl ratio >0.95 for all the scan positions within 3 deg of the optical axis. For larger angles, there is increasing astigmatism, but even at 5 deg the system remains diffraction limited (RMS er-

ror $<\lambda/5$) except for small defocus changes. The contribution to aberrations from the refractive afocal relay was not included in this calculation since it was negligible, although the measurements include the first of the two lenses (see below).

As a result of this design, the final stage of the system requires a large FOV to allow both for imaging different regions of the retina to create a montage and for compensation of eye movements. This was not readily achieved with an all reflective design. For this reason we used a pair of on-axis lenses for the final relay pair. This pair forms a Badal optometer. By changing the distance between these two lenses, we could alter the focus of the system without changing the position of the exit pupil. In principle, either a pair of off-axis parabolic mirrors or high-quality lenses could be used to ensure diffraction limited performance over the entire FOV (see below). For cost reasons, we chose traditional spherical lenses. The distance between the lenses was varied by mounting the entire AOSLO section, except the final lens, on a $2' \times 2'$ (1 ft = 30.48 cm) optical breadboard (dashed line on Fig. 1), which in turn was mounted on a movable stage under computer control. Thus, major defocus errors were corrected by the Badal system, preserving the stroke of the deformable mirrors for both higher-order corrections and small focus changes. It should be noted that some of these changes come about because the afocal relay (L1 and L2) has unconnected Petzval curvature, but this is equivalent to defocus error over the small imaging field, which can be corrected within the loop by our system (see Section 3). This was confirmed by the Zemax ray trace calculation for different configurations of the first afocal relay.

We measured the performance of the optical system by placing a paper target in the first retinal plane (between the two relay lenses L1 and L2) and measuring the wavefront using different positions of the scanners.

B. Detection Channel

Most of the near-infrared light returning from the retina passes through the beam splitters arrives at the light collection lens and then is focused onto a retinal conjugate plane. At this plane is located one of eight different confocal stops. The stops are mounted on an aperture wheel, which is positioned using a stepper motor, allowing rapid interchange of the apertures. The stepper motor is in turn mounted on a computer controlled XY stage (Thorlabs), which allows precise positioning of each aperture. Light that passes through the confocal aperture is then imaged onto an RCA avalanche photodiode (APD) with custom electronics.²⁴ This detection arrangement allows us to build up an image that ranges from tightly confocal ($0.87\times$ the size of the diffraction-limited Airy disc) to wide open ($120\times$ the size of the Airy disc). In addition each confocal aperture can be translated, allowing us to measure the image returning from the retina for different portions of the double pass psf. The signal from the APD system is input directly into a data translation 3152 imaging board to form the video image. For the current work, the video board is clocked at 8.4 MHz (512×512 image at 15 frames/s), but it can run up to 1024×1024 at 30 frames/s (16.8 MHz pixel clock). The typical high-resolution field size is about $1.25^\circ\times 1.25^\circ$ on the retina, but data can be collected at larger, less-magnified FOVs with a simple electronic adjustment. This adjustment does not alter the optical resolution of the system, however.

C. Wavefront Sensor and Wavefront Control

Wavefront sensing is performed using the Shack-Hartman sensor (SHS) (Fig. 1) based on a 12-bit sensor (Uniq Vision 1820) cameralink camera. The SHS included a lenslet array with approximately 450 samples within a nominal pupil of 6 mm (on the eye). This pupil is slightly smaller than in many AO systems and was chosen since we designed the system for use in older patients. The array sampling is chosen such that each actuator of the deformable mirror is covered by four lenslets. This allows us to minimize the effects of waffle mode error. In addition, the denser sampling allows us to eliminate measurement spots that have very low power, which can occur in older subjects due to local lens changes, and that occur along the edges of the pupil due to slight head movements since the wavefront is oversampled by the lenslet apertures. The WFS beacon is provided by a 680 nm SLD with 50 μ W input into the eye through a 5% coupler (Fig. 1, BS2). The size of the beacon light at the pupil of the eye was 1 mm. We chose 1 mm for several reasons. A small pupil provides a large depth of field for the beacon, and since one goal is to image retinal diseases where there may be considerable retinal thickening, having the beacon in focus, even when imaging far from the plane of maximum reflectance, was considered advantageous. Another advantage of our optical configuration is that the beacon is located away from the center of the pupil, minimizing the effect of corneal reflections. In a WFS, reflections can provide severe biases in estimating the wavefront, and these reflections are compounded in a system that is performing retinal stabilization, since the retinal field is moving dynamically. This issue is covered in more detail in Section 4. BS2 introduces the light for the WFS

between the eye and the DM. This location is used to minimize the impact of local changes in the DM shape on the shape of the retinal beacon. While this is not necessary for a beacon with a large pupil, a small pupil can be very rapidly effected by changes in the control of a single actuator, potentially resulting in large and rapidly changing alterations of the quality of a small spot.

Wavefront control is performed by a MEMS DM (Boston Micromachines, Inc.) with a 4.4 mm aperture, 140 actuators (400 μ m center-to-center actuator spacing), and 4 μ m of stroke. The control algorithm uses the following approach. First, the SHS was calibrated by injecting a wavefront into the system at BS1 that was diffraction limited, except for 0.2 diopters of spherical error. This wavefront was generated by placing a point source at 5 m. Then a reflective sample was introduced at the first retinal relay, and the influence function of the system was measured by determining the relation between moving a single actuator and the SHS response. Actuators that have no influence on the image formed by any of the SH lenslets within the pupil are eliminated, as are lenslets for which no actuator influences the position of the image produced by the lenslet. The resulting matrix was inverted using a singular value decomposition with a Tikhonov regularization³⁵ for correcting the possible amplification of small noise induced error in the inverse. During imaging the SHS obtains images that are synchronized to the scan system (see below). Centroids are calculated in a shrinking box approach³⁶ for each region in the SH image that is included in the control matrix. These are differenced from calibration locations identified during system calibration to produce a matrix of slope estimates. In addition, areas in the pupil for which the lenslet spots are poor, as can occur due to movement of the pupil edge or local changes in the lens of the eye, are determined on the fly by using a simple statistic that reports the presence or absence of a "spot." If a spot is missing or very weak, we first place zeros into the slope table for that location. We then low pass filter the slope matrix, which changes the erroneous zeros toward the average of the surrounding estimates of the slopes (from good lenslets). We finally substitute in the original "good" slope values at their original locations. This approach allows us to rapidly deal with missing centroids within the real time loop. These slope estimates are then used in a simple proportional control loop.³⁷ To allow real time focus changes using the MEMS mirror, we use a slope displacement technique. Since defocus produces a change in slope that is proportional to the distance from the center of the pupil, we can simply create a distance matrix corresponding to each SHS lenslet. Defocus is then varied by multiplying this matrix by a gain (the defocus value) and adding the resulting matrix to the displacement matrix from the SHS.

Each SHS image was integrated for 30 ms, synchronized to the start of each imaging field. Processing was performed as soon as a frame was acquired and required approximately 30 ms. Thus, images were acquired during the first half of a scan and were processed during the second half of each frame, and the mirror was updated before the start of the subsequent frame (and the next SHS image acquisition). Displays were either updated during

spare time, or they could be continuously updated, which slowed the loop somewhat.

D. Wide-Field Retinal Imaging

The principles and performance of the wide-field imaging system have been previously described.^{31,38,39} It is a confocal, tracking line-scan SLO (TSLO, Fig. 1) that in the current implementation uses an imaging wavelength of 920 nm. The wide-field imaging system and the AOSLO imaging beams are combined with a dichroic mirror, which is placed directly in front of the subject's eye (Fig. 1, BS3). Thus, the wide-field imaging system and eye tracker have only this single optical element in common with the AOSLO. This separation was necessary to facilitate the very different optical requirements of the two systems. As a result, the range of positions over which the AOSLO imaging field can be placed in relation to the wide-field imaging FOV is determined by the relation of the apertures of L1 and L2, which subtend a much smaller angle (~ 12 deg), and the position of the wide-field image (~ 35 deg). In practice we cannot achieve the full 12 deg range for the AOSLO, since the field is apodized at the edges.

E. Retinal Tracking and Stabilization

The tracker is designed to stabilize the location of the illumination light on the retina with respect to a specific retinal feature in a manner similar to the method described previously.^{31,38,39} In the current implementation we have changed several parameters to adapt it for use with the AOSLO. The tracker is a confocal reflectometer that illuminates the retina with a $30\ \mu\text{m}$ spot of light (1064 nm). This spot revolves in a circle at 16 kHz, forming a "donut" of illumination on the retina. Light returning from the illuminated region is detected by an indium gallium arsenide APD, and the response is measured using narrowband phase-sensitive detection. Thus, the phase of the response provides information as to the pattern of retinal reflectivity along the donut-shaped path of the illuminating beam. This signal provides the input to a digital signal processor (DSP), which implements the tracking algorithm and operates control circuitry to deflect and maintain the donut on the retinal feature chosen. The retinal feature is typically the center of the optic nerve head but can be any feature with high contrast in two dimensions. The polarity of the tracking feature can be software controlled, allowing tracking of dark features such as vessel crossings. Since the wide-field imaging optics reflect off the same tracking mirrors, the wide-field image is stabilized at the same time. However, the AOSLO image must be controlled separately. The DSP provides control voltages to the steering galvanometers (SG1 and SG2, Fig. 1). The control voltages are scaled and filtered versions of the voltages controlling the tracking, with the scaling and filtering set by the user during calibration. Offsets can be added to the steering mirrors to change the relation between the tracked feature and the center of the imaging field, which allows the high-resolution imaging system to image over a retinal range of 10 deg by changing the relation between the imaging and the tracking beams.

F. Calibration of the Tracker for AOSLO Stabilization

Because of the separation of the optics between the wide-field and the AOSLO imaging systems, the tracking system must control the steering mirrors to position the AOSLO beam. This requires calibration of the system *in situ*. The goal is to set a relation between the internal tracking mirrors of the TSLO and the steering galvanometers of the AOSLO. Since both can be calibrated to match changes in external angles with voltage, in principle this only needs to be done once. To perform the calibration a subject's retina is first imaged with both systems operating. With tracking turned on, the subject alternately fixates the top, bottom, left, and right of a target that was approximately 2 deg in diameter. During the horizontal eye movements, the amount of displacement of the high-resolution image was measured for the horizontal direction. The gain was then changed to increase or decrease the displacement, iteratively and in conjunction with a similar vertical calibration, until the position of the AOSLO image of the retina before and after a fixation shift was the same.

G. System Control and Electronics

The electronic control of the system is implemented as three subsystems on separate computers that allow the operator to select a region of interest, correct the wavefront aberrations for that retinal location, and acquire a highly magnified image at high sampling density (Fig. 2). The AO computer system receives start-of-frame synchronization signals from the D/A converter, which drives the slow-scan galvanometer, acquires an SHS image, and then computes the resulting mirror control signals. While waiting for the next acquisition signal, the AO control computer updates the computer display, including wavefront error estimation, SHS deflection map, and a mirror deflection map. The entire loop runs at roughly 10 Hz. The AO control computer receives control input from and provides control state information to the imaging computer via TCP/IP interface.

The tracking computer provides a wide-field image of the eye and the controls necessary to move the highly magnified AOSLO FOV to a desired region of interest. This is performed by adding an offset to positions of the steering mirrors. This offset is then summed with a scaled version of the retinal motion signal to provide a signal that causes the AOSLO image to track the retina. The tracking computer also controls real time wide-field imaging, including video acquisition and storage, and provides the control information and an interface to the DSP,^{7,40} (Fig. 2) but it does not influence retinal illumination or image acquisition timing, gain, or any function other than location.

The imaging computer is responsible for directly controlling image acquisition and the imaging system state, including photodetector gain, focus, aperture selection and position, and position of the slow-scan galvanometer. The slow-scan galvanometer voltage signal is obtained from a programmable D/A converter, which also provides start-of-frame synchronization signals to the frame grabber and to the SHS sensor in the AO control system. In

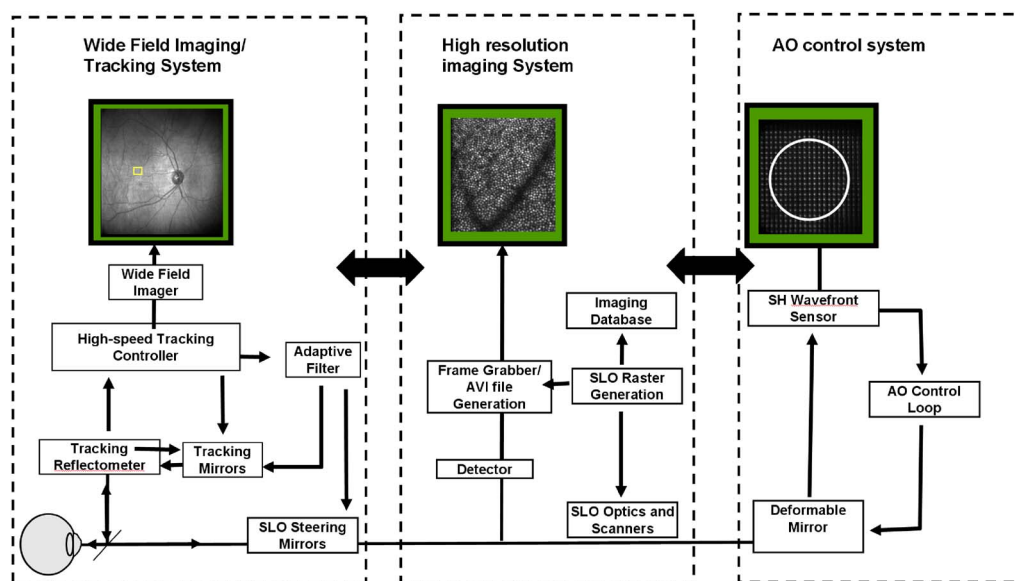


Fig. 2. (Color online) Partition of imaging system control between systems. Dashed lines represent the three major control subsystems, the wide-field imaging/tracking system (left), the high-resolution imaging system (center), and the AO control system (right). The high-resolution imaging system controls standard operational parameters of the other two systems via IP (double black arrows).

addition this system indirectly controls the AO computer and tracking computer via IP links (Fig. 2). These links provide control for all standard operating interventions, although it is necessary to initialize the AO control and tracking control on their host computers at the start of an imaging session. The imaging computer also is responsible for recording the system state into a database, for rapid retrieval of relevant system information, by performing a timed video acquisition in real time, consisting of acquisition of between 2 and 2^8 sequential frames. All state information concerning the detection channel is stored on the imaging computer, along with a pointer to the position in the audio-video interleave (AVI) image file, and the AO computer status concerning the state of the AO control loop. The AO information includes both the RMS error of SH centroids and the Zernike coefficients through the seventh order. This state of the tracking system is also recorded, including whether the tracking control is on or off and the offset of the steering mirrors to indicate retinal location. The imaging computer can also instruct the tracker to record a video sequence and provide a name for the sequence that is recorded in the database.

Image montaging and correction for sinusoidal distortion are performed offline, using an AVI file browser that was developed in MATLAB (Mathworks, Inc.). This browser has a GUI that allows browsing through an AVI file while simultaneously providing imaging details for each frame from the imaging database. Frames are marked using the browser by building a list of frames. Once a series of images is chosen, the software reads them into MATLAB, applies a polynomial dewarping algorithm to remove the sinusoidal warping, and places all of the selected images both into the MATLAB workspace and into a PowerPoint file for manual alignment. While the galvanometer control voltages are recorded in the database, the software has not yet been developed to make this process automatic.

This system design results in a session that typically matches the following sequence: Subjects are first aligned using the wide-field imaging system. The tracking system is then engaged, and individually dependent parameters are set, such as the feature to be tracked and the tracking gains. For all data in the current study, the optic nerve head was used as a tracking feature. Once set up and tracking, the system can then be controlled remotely from the imaging computer. The focus of the AO system is then set using the Badal optometer. When the desired focus is achieved, such as near the plane of the photoreceptors, the AO control is engaged, and fine control of the Badal optometer is used to minimize the stroke of the MEMS mirror. At this point, it may be necessary to introduce additional trial lens correction into the system if the MEMS mirror cannot adequately compensate for astigmatism or if there is not a sufficient range in the Badal optometer to compensate for spherical errors. These trial lenses are located next to the steering mirrors. The location of these trial lenses away from a pupil conjugate can cause some problems with the tracking system, as detailed in Section 4. Once the AO control loop is locked, the retinal features of interest are imaged by moving the steering mirrors or controlling the detection and AO system as appropriate.

H. Subjects

We have tested eight subjects with the system, ranging from 21 to 56 years in age. All subjects except two had normal retinal status. Patients with retinal disease include an individual with recurrent central serous retinopathy and one with epiretinal membranes. The study was approved by the Indiana University Institutional Review Board. Light safety was calculated based on ANSI standards⁴¹ and a recently published procedure for ophthalmic instruments.⁴² All subjects provided informed consent before participating in the study.

3. RESULTS

A. Optical System Performance

The system had excellent optical properties, allowing the dynamic range of the MEMS mirror to be used to correct eye aberrations. A Zemax wavefront estimate of the on-axis performance is shown in Fig. 3(a) and predicted performance at 5 deg is shown in Fig. 3(c). Figures 3(b) and 3(d) show the corresponding measured wavefronts. These were measured using the SHS, with a target placed at the first retinal conjugate (at the focus of the Badal system) for both the on-axis and 5 deg off-axis locations. On axis, the system is essentially diffraction limited, with an RMS error of $\lambda/10$. When the steering mirrors are displaced to the 5 deg position, the measured wavefront aberrations are worse, with an RMS error of approximately $\lambda/5$. This increased aberration is almost purely astigmatism.

B. Wide-Field Imaging Performance

Wide-field imaging has been previously described.^{31,43} The current implementation uses a longer-wavelength imaging beam (920 nm) and an additional optical component, and the images appear slightly noisier. This appears to occur due to both the decreased transmission of water at 920 nm and the decreased sensitivity of the line scan CCD camera. However, the use of 920 nm for wide-field imaging facilitates the combination of the wide-field imaging beam and the AOSLO imaging beam (with a wavelength band centered at 840 nm), using a dichroic beam

splitter. An unintended benefit of using these two closely spaced wavelengths for imaging is that some of the long wavelength signal of the AOSLO beam is seen as a bright area on the wide-field image, providing live confirmation of the location of the high-resolution image.

Figure 4 compares views of the same retina from the wide-field imager (left) and a montage of AO images obtained from a 56-year-old male subject with epiretinal membranes, showing dark structures in the AOSLO unanticipated from the view provided by the wide-field imager and not found in normal retina. The wide-field image contains a bright region (long arrow) arising from light from the AO imaging being collected by the line scan detector (it is bright due to the longer integrating time of the line scan detector). This bright region slowly moves (due to aliasing from the differing frame rates of the two systems). The AOSLO images were focused in the plane of the photoreceptors, and each image in the montage was generated from a single frame without signal averaging. The montage was generated by adding displacements to the steering mirrors that move the AOSLO system, allowing us to obtain images from a number of locations rapidly. The right panel shows a second region of retina in this subject, emphasizing retinal striae. To move the imaging location, the fixation point was moved and an offset was applied to the steering mirrors control voltages. The images were then aligned by the operator after the session was complete.

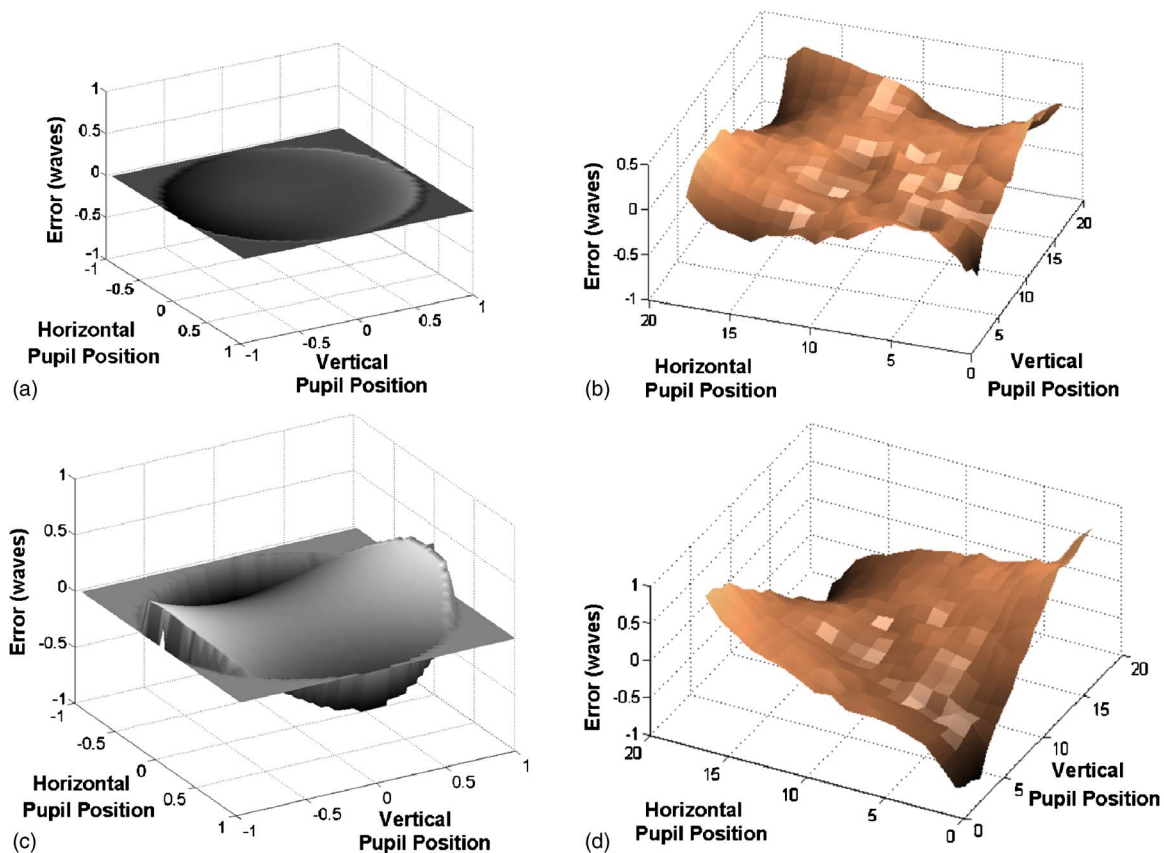


Fig. 3. (Color online) Comparison of predicted (left column) and measured (right column) wavefronts for the optical system. Calculations were performed for both on-axis (top row) and 5 deg off-axis (bottom row) field positions. Measurements were made by placing a target between L1 and L2 (Fig. 1) and using the SH WFS to measure the aberrations.

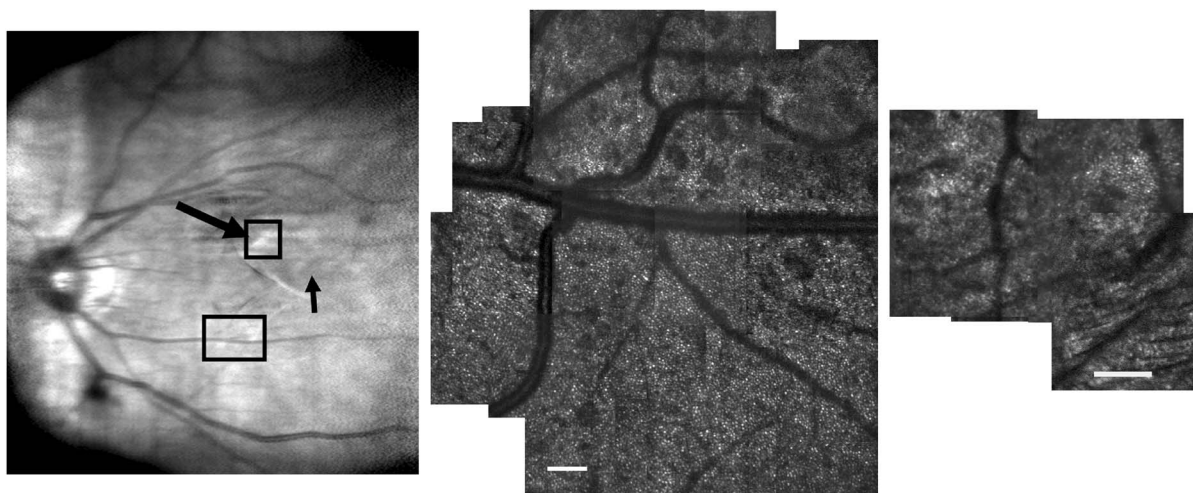


Fig. 4. Imaging data from a 56-year-old male with an epiretinal membrane. Left: Near IR (920 nm) view of the retina, obtained from the wide-field imaging system. The boxes show the approximate locations of high-resolution retinal montage (center and right). The short arrow shows the location of the fovea. Retinal traction due to the epiretinal membrane is visible in the center of the field. Center: An 840 nm AO retinal montage generated by using the tracking mirrors in the AO system to offset the retinal location being imaged. Data were generated in about 2 min, once the subject was aligned and the AO was adjusted. Individual frames were aligned manually offline. Confocal aperture was $2.6\times$ the diameter of the Airy disc. The scale bars represent $100\ \mu\text{m}$. Right: AO images, gathered in the same way as the center image but for a different region of the the retina. These frames show detail of the region along the outer edge of the epiretinal membrane with stria in the lower right corner. The scale bars represent $100\ \mu\text{m}$. The confocal aperture was $2.6\times$ the diameter of the Airy disc.

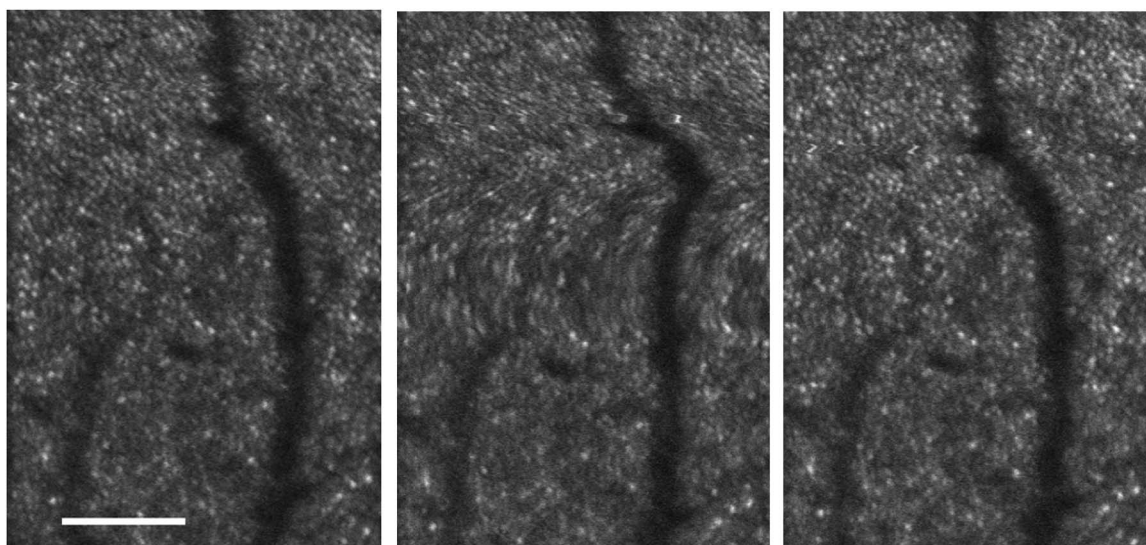


Fig. 5. Example of eye tracker compensation for small saccadic movements. In the middle frame a saccade was initiated, and the retina began to slew (right moving then left moving blur in top and middle of frame). The eye tracker compensates, with a slight delay, and by the bottom of the middle frame the correct retinal position is again achieved, and the third frame is well aligned to the first. Residual small motions remain as described in the text. Scale bar is $100\ \mu\text{m}$.

C. Tracking Performance

To avoid amplifying the noise in the tracking system, and possibly cause ringing, we adjusted the high-frequency cutoff of the control system for the steering mirrors to 200 Hz. Because of this, the eye tracker did not keep up with saccades. Figure 5 is an example of three successive AOSLO frames obtained while the eye tracker was operating. During the second frame (middle panel) there was a small saccade. This appears as a tearing of the image, i.e., retinal movement to the right, followed by a rapid return when the eye tracker corrected the resulting error in

the retinal image. By the third frame the image is returned to approximately the original position on the image frame, although the eye has actually rotated between the first and third frames.

We quantified this tracking performance by obtaining a sequence of image frames with image stabilization turned on. A series of 10 within-frame locations, spanning the image frame, were defined in the first frame. A local subregion around each of these locations was then cross correlated with each of the subsequent frames. For each cross correlation, the peak of the cross-correlation function was

taken as the region of optimal alignment. We then calculated displacements as a function of time for all 10 locations. Figure 6 shows the results of this analysis for an observer with relatively poor fixation. In this subject, the computations described could not be carried out without the stabilization, since many frames would contain images outside the bounds of the first image. With eye tracking we find that the modal displacement is $6\ \mu\text{m}$, 50% of the time the images are within $10\ \mu\text{m}$ of the mean position, and 90% of the time images are within $18\ \mu\text{m}$. The long tail of the distribution represents position estimates during saccades and the resulting large displacements, as shown in Fig. 6. The actual estimate of the error using this quantification scheme is not accurate for these periods during active saccades, since the cross correlation will not have accurately determined the true motion. However, while this may affect the averages reported, it does

not change the distribution estimates, except that the error for the large values probably represents a lower bound rather than the true value.

D. Adaptive Optics Imaging Results

When operating on the eye, the AO system was effective in improving image quality. Figure 7(A) shows single-frame images for a male subject, aged 22 years, with a correction of 4 diopters with the AO turned off. Figure 7(B) shows an image of the same subject and retinal location with the AO on. In subjects with sufficiently low aberrations we could also use the deformable mirror to rapidly change the plane of focus. Figures 7(C) and 7(D) show images from a 56-year-old male subject with recurrent central serous retinopathy, obtained with the best focus at

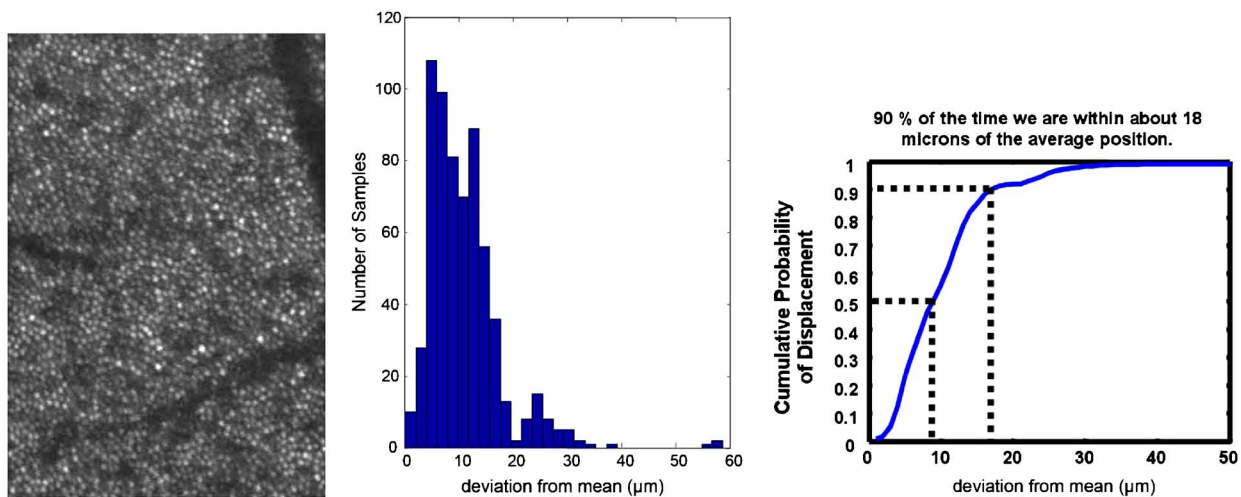


Fig. 6. (Color online) Accuracy of retinal image stabilization was measured using the AO system. A short video sequence was recorded in a normally sighted subject with low fixation stability (left panel). Cross correlation was then used to measure the shift in location of eight points within a frame, over about 10 s of video. This includes two small saccades and considerable eye drift. The center graph shows the histogram of the displacements measured (using the average position as the standard). The right graph shows the cumulative probability for a given location to move. During untracked epoch, this procedure could not be used, since the frame had numerous excursions larger than the image region. This means the eye movements were often greater than $100\ \mu\text{m}$.

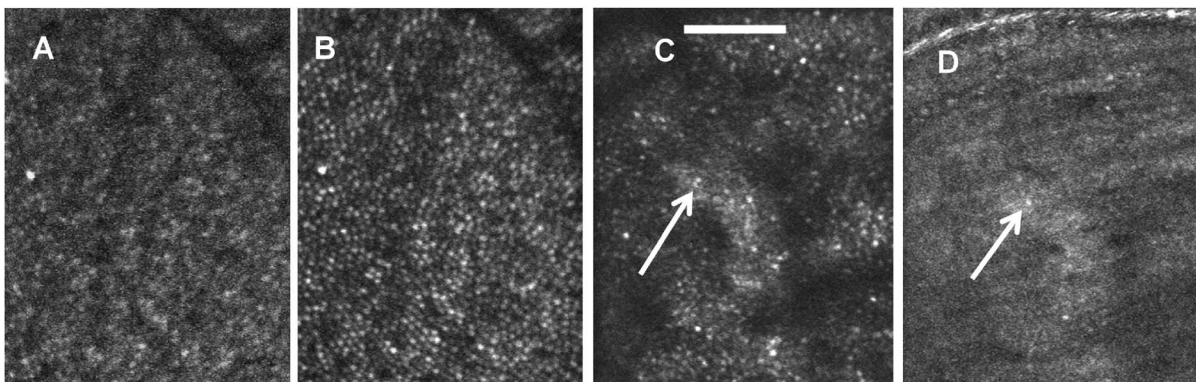


Fig. 7. Example of the imaging performance of the AO system. All images are single frames of video. A, Uncorrected, best-focus image of the retina of a 43-year-old female subject. B, Same region of retina, but with the AO control loop activated. Note the increased contrast of the cones, with all cones within the field now resolved. C, Image of the retina of a 56-year-old male with recurrent central serous retinopathy, with AO control activated. C, System is focused at the level of the cone photoreceptors, showing areas of strong cone light return and areas with poor cone light return. The white bar represents $100\ \mu\text{m}$. D, Same region of the retina, focused at the nerve fiber layer. Small retinal vessels are visible, and the continuous nature of the inner retinal surface is evident. White arrows show corresponding retinal locations for images C and D.

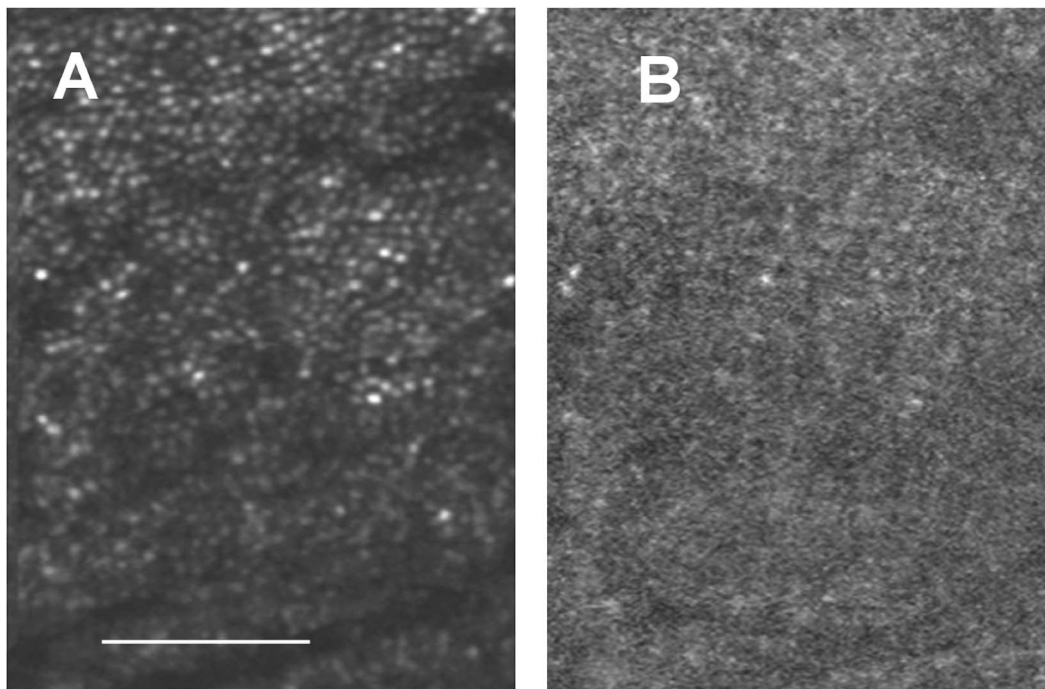


Fig. 8. Example of the effect of displacing the confocal aperture: A, AO control active, aperture aligned; B, AO control active, aperture displaced $2\times$ the Airy disc radius.

the level of the cones and the nerve fiber layer (respectively) and by changing the curvature of the deformable mirror.

Displacement of the confocal apertures produced marked changes not only in the intensity of light detected but also in the image contrast of different features. Figure 8 shows a region of retina imaged with an aperture diameter $2.7\times$ the diameter of the Airy disc. The left image shows the resulting AOSLO image when the confocal pinhole was aligned to the psf; the right image was obtained with the aperture displaced by twice the aperture's radius. In the aligned image, cones are readily apparent at high contrast. In the displaced aperture condition, cones are mostly not visible. Figure 9 shows the interaction of the AO control with aperture displacement for a 43-year-old female subject. In these six images the aperture has been moved systematically from aligned (left column), to displaced by $1\times$ the radius (with the edge of the aperture on the center of the psf; middle column), and displaced by $2\times$ the radius (right column). This was done for both AO-on (top row) and AO-off (bottom row) conditions. The left column therefore shows the now traditional AO-on/AO-off comparison. The image in the top left has been scaled down in intensity by a factor of $0.5\times$ for display. Corrected for the gain of the APD, the mean intensity over a region of 25,754 pixels for AO-on was 85.3 gray-scale units (± 41.8), the intensity with AO-off was 38.0 (± 15.2). That is, the average intensities differed by more than a factor of $2\times$, and the standard deviations by $2.8\times$, due to the high contrast of the cones with AO-on. Thus, the AO-on condition is brighter and sharper, as expected. With the aperture displaced by $1\times$ the radius, there is a much smaller effect of AO; the intensities decrease to 48.5 (± 20.2) and 34.8 (± 13.4) for AO-on and AO-off, respec-

tively. Thus, cone contrast is still improved, but the image is dimmer than for the centered aperture owing to the rapid drop in the psf in the AO-on condition. With AO-off, there is not much difference between the centered and the displaced apertures, indicating that the double pass psf is broad. Finally, with the apertures displaced by twice its radius, the AO-on condition is quite dark (25.4 ± 10.7), and the AO-off condition is slightly brighter (26.6 ± 11.12). That is, turning on AO control decreases the amount of light in the tails of the psf, as expected. However, the image does not go completely dark. As has been previously shown,^{20,21,44,45} some features show up well in multiply scattered light.

The effect of multiply scattered light is also shown in Fig. 10, where we show the effect of changing the size of the aperture on the retinal image. The set of four images (A–D) are of a region of retina from a 56-year-old male subject that includes a set of small blood vessels. The first three images (A–C) show the effect of changing focus with a confocal aperture $4\times$ the size of the Airy disc, moving from the photoreceptor layer (A) to the inner retina (C). Figure 10(D) shows the same region with a large ($26\times$ the Airy disc diameter) aperture, with areas of scattering being bright. Figures 10(E) and 10(F) demonstrate the effect of increasing the aperture size in an eye with retinal pathology. Here we compare images from the retina of a subject with an epiretinal membrane. The confocal view, with a pinhole $2.6\times$ the size of the Airy disc [Fig. 10(E)] shows a region where the membrane is folded. The open confocal (large aperture, $>50\times$ the size of the Airy disc) view shows that there is considerable scattering in some of these regions, which leads to a large return of light through the region of retina surrounding the small aperture.

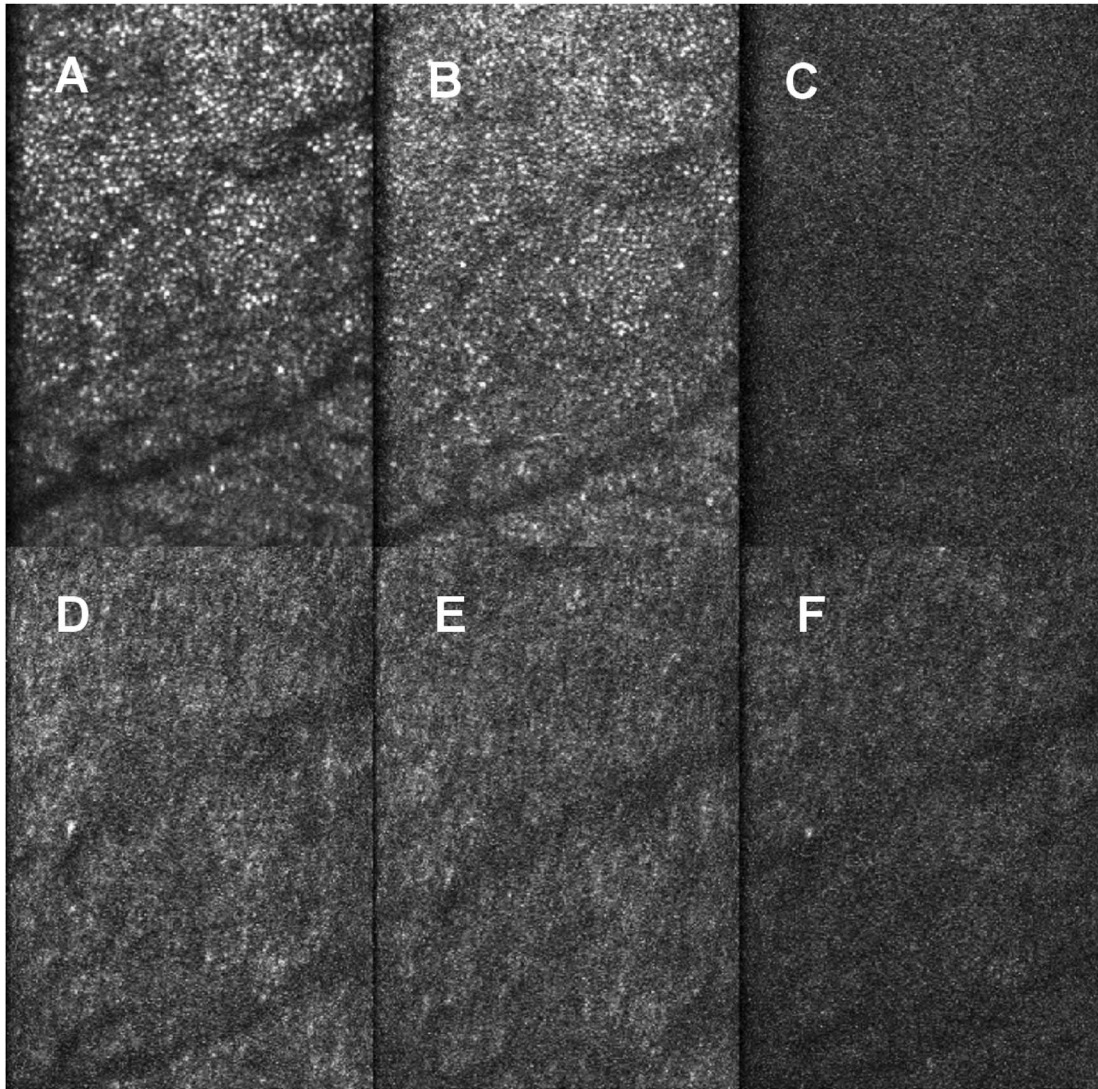


Fig. 9. Example of the interaction of displacement of the confocal aperture with adaptive optics control. Images A–C were obtained with the AO system activated and with successively larger displacements of the aperture from the peak of the Airy disc. A, Aligned aperture, $2.6\times$ the Airy disc diameter, centered on the Airy disc. This image has been scaled down in intensity by $2\times$ to allow it to be printed at the same level as the other five images. B, Same aperture, displaced one radius of the aperture, that is, with the circumference of the aperture on the center of the Airy disc. C, Same aperture, but now displaced by 1 diameter. D–F, Same positions of the apertures as A–C, respectively, but now with the AO control system off. While the AO system increases the intensity for the aligned aperture, it decreases intensity for the misaligned aperture.

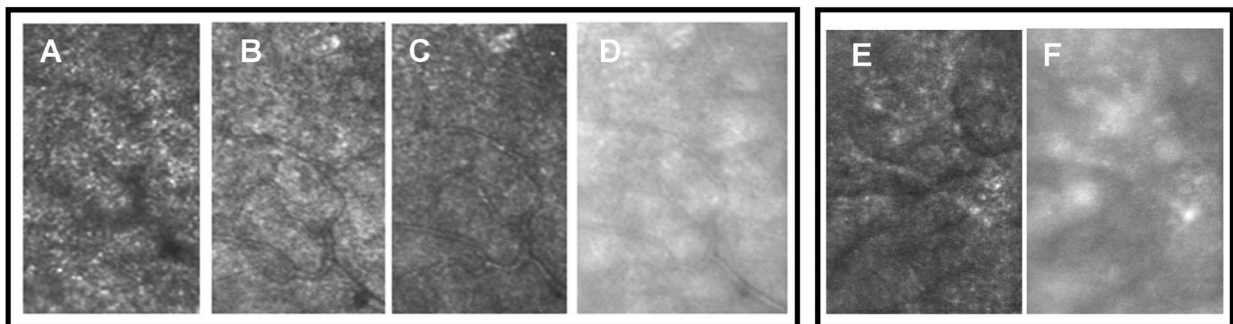


Fig. 10. Images from a 54-year-old Caucasian male showing the effect of confocal aperture size on imaging performance of the AO system. Images A–C were obtained using an aperture $2.6\times$ the size of the Airy disc, focused at different retinal layers ranging from just above the photoreceptors (A) to the level of the outer capillaries (C). Image D was obtained with an aperture $26\times$ the size of the Airy disc. Images E and F are from a 56-year-old male with an epiretinal membrane. The images are obtained with the AO system active and with the focus adjusted to the surface of the membrane. Here we see the rough surface and fold of the membrane in image E. Image F, obtained with a large confocal aperture, shows increased scattering from several structures within the membrane.

4. DISCUSSION

We have described a system that allows us to generate diffraction limited images of the human retina while simultaneously tracking and stabilizing the retinal view in the presence of eye movements. The optical system maintains diffraction limited performance over a large FOV by using primarily reflective optics, thereby minimizing ghost reflections and providing achromatic performance. Refractive elements, which do introduce unwanted reflections (see below), are used only in the first afocal relay.

The current system is able to dynamically change both focal plane and the degree of confocality, allowing us to make precise biophysical measurements of the scattering of light in the retina, as well as precise anatomical information on the microscopic detail of the human retina in both normal and pathological eyes. Our system has unique features that allow it to be used to make measurements that are not commonly obtained from AO systems. Specifically, the ability to rapidly and reliably change the position and size of the confocal apertures allows us to quickly quantify spatial aspects of retinal light scattering. We showed that in normal retina the contrast of the cone photoreceptors drops rapidly to less than 10% as the confocal aperture is misaligned. Thus, controlling the apertures allows us to sample different types of structures. In this case of a normal retina, light that is multiply scattered passes through the retina in the tails of the retinal psf. This occurs as a result of two processes. First, light singly scattered far from the plane of focus will have a large blur circle; and second, because multiple scattering, which occurs in the retinal pigment epithelium (RPE) and choroid will be more widely distributed in the retina, depending on the scattering length. In near-infrared light, much of the light returning through the pupil has penetrated into the choroid.^{46–48} The lack of cone contrast in the tails of the psf is consistent with the findings of Prieto *et al.*⁴⁹ that light from the RPE is not guided toward the pupil. However, Choi *et al.*⁵⁰ have argued that the cones guide light impinging on them from the sclerod direction.

The eye tracker/stabilizer provided two benefits. First, it is helpful when imaging an eye to have a context for the high-resolution images. When viewing the small-field AO images, it is often nearly impossible to be sure where a new subject is actually fixating, unless it is possible to see the fovea. The incorporation of the wide-field imaging system provides information to the experimenter on the retinal region under examination and its relation to the whole posterior pole. The image stabilization is also useful. Errors arise in the tracking due both to noise and to the displacement between the tracked feature and the region being imaged at high resolution. While torsional motions of the eye are relatively small at the scale of the AO images, they can become important, and the stabilization is currently limited to translational motions. Nevertheless, while the stabilization is not perfect (co-adding multiple frames without any intervening processing is not possible), it is sufficiently good that relatively simple software routines can operate unattended and align all images from a given nominal region and image type. It also allows us to directly compare very different image types for the same region, where features become difficult to re-

late, even when only the plane of focus is shifted (see Figs. 7(C) and 7(D)). Automatic frame rejection routines to detect frames or subframe areas with saccadic transients within them (Fig. 5) are not yet implemented. Such movements degrade the local cross correlation of frames, and thus automated software should be able to perform this task, and more sophisticated dewarping algorithms²² would be a beneficial adjunct to the hardware-based tracking to remove the remaining distortions.

A related advantage of the system is that by adding offsets to the steering mirrors, the angle of the beam at the pupil can be rapidly changed, thereby shifting the retinal region being imaged. Thus we can rapidly obtain multiple views of the retina that can be stitched together relatively simply. However, since these steering mirrors are conjugate to the center of rotation of the eye (approximately) but not to the pupil, they cause an appropriate change in pupil position for rotations of the eye, but an inappropriate pupil motion for a translation of the retinal image. This limits the range over which we can scan the beam without recentering the eye. This issue will be addressed in the future by adding the offset to our fast- and slow-scan mirrors.⁷

A secondary problem arises from the interaction of the retinal tracker with the current AOSLO first afocal relay optics (the Badal optometer). As the high-resolution FOV is steered across the retina, lenses L1 and L2 (Fig. 1) produce reflections as the beam crosses the apex of the lenses. These reflections can degrade the wavefront sensing owing to the low numerical aperture and the resulting high depth of field of the SHS. Additionally, where a large retinal conjugate aperture is being used, the reflections can also intrude into the retinal image. Most AO systems have a fixed FOV, and therefore system reflections can either be designed out, e.g., working slightly off axis with the beacon, or be subtracted from the SHS. In a system where the imaging angle is dynamically changing, these reflections are not constant and therefore cannot be subtracted. Future implementations would be better served by using a reflective system to implement refractive correction, either by using a high-stroke deformable mirror⁵¹ or a Badal system composed of mirrors.

Finally, the manner of introducing refractive corrections into the system is important. Because we keep the two image channels separate, focus and field sizes are independent, and the relative gains of the retinal steering mirrors for each system are different, but fixed. However, if we introduce correcting lenses (for astigmatism or high levels of ametropia) into our system, and they are not precisely at a pupil plane, then we change the relative magnification between the two systems. While this change is not critical for the imaging, it also changes the calibration relation between the tracking system and the steering mirror deflections, and a correction factor must be introduced.

In summary, we have described what is to our knowledge a new, MEMS-based AOSLO. This system has been designed to work with active retinal stabilization and to provide simultaneously a high-resolution AO view of the retina and a lower-resolution, wider-field view of the retina. We have incorporated a flexible detection channel in the system and have shown that this type of detection

channel allows direct measurement of the contribution of different light paths to the retinal image.

ACKNOWLEDGMENTS

This work was supported by NIH grants RO1 EY04395 and EY014375. We thank Hongxin Song, Xiaofeng Qi, and Zhangyi Zhong for help with some of the data collection, and Dan Sumorok for programming contributions.

Corresponding author Stephen A. Burns can be reached by e-mail at staburns@indiana.edu.

REFERENCES

- J. Liang, D. R. Williams, and D. T. Miller, "Supernormal vision and high-resolution retinal imaging through adaptive optics," *J. Opt. Soc. Am. A* **14**, 2884–2892 (1997).
- A. Roorda and D. R. Williams, "The arrangement of the three cone classes in the living human eye," *Nature* **397**, 520–522 (1999).
- A. Roorda, "Adaptive optics ophthalmoscopy," *J. Refract. Surg.* **16**, S602–S607 (2000).
- J. F. Le Gargasson, M. Glanc, and P. Lena, "Retinal imaging with adaptive optics," *C. R. Acad. Sci., Ser IV: Phys., Astrophys.* **2**, 1131–1138 (2001).
- A. Roorda, F. Romero-Borja, W. J. Dornally, H. Queener, T. J. Hebert, and M. C. W. Campbell, "Adaptive optics scanning laser ophthalmoscopy," *Opt. Express* **10**, 405–412 (2002).
- S. A. Burns, S. Marcos, A. E. Elsner, and S. Bara, "Contrast improvement of confocal retinal imaging by use of phase-correcting plates," *Opt. Lett.* **27**, 400–402 (2002).
- D. X. Hammer, R. D. Ferguson, C. E. Bigelow, N. V. Iftimia, T. E. Ustun, and S. Burns, "Adaptive optics scanning laser ophthalmoscope for stabilized retinal imaging," *Opt. Express* **14**, 3354–3367 (2006).
- Y. H. Zhang, S. Poonja, and A. Roorda, "MEMS-based adaptive optics scanning laser ophthalmoscopy," *Opt. Lett.* **31**, 1268–1270 (2006).
- D. C. Gray, W. Merigan, J. I. Wolfing, B. P. Gee, J. Porter, A. Dubra, T. H. Twietmeyer, K. Ahmad, R. Tumber, F. Reinholz, and D. R. Williams, "*In vivo* fluorescence imaging of primate retinal ganglion cells and retinal pigment epithelial cells," *Opt. Express* **14**, 7144–7158 (2006).
- B. Hermann, E. J. Fernandez, A. Unterhuber, H. Sattmann, A. F. Fercher, W. Drexler, P. M. Prieto, and P. Artal, "Adaptive-optics ultra high-resolution optical coherence tomography," *Opt. Lett.* **29**, 2142–2144 (2004).
- R. J. Zawadzki, S. M. Jones, S. S. Olivier, M. T. Zhao, B. A. Bower, J. A. Izatt, S. Choi, S. Laut, and J. S. Werner, "Adaptive-optics optical coherence tomography for high-resolution and high-speed 3D retinal *in vivo* imaging," *Opt. Express* **13**, 8532–8546 (2005).
- E. J. Fernandez, B. Povazay, B. Hermann, A. Unterhuber, H. Sattmann, P. M. Prieto, R. Leitgeb, P. Ahnelt, P. Artal, and W. Drexler, "Three-dimensional adaptive optics ultra high-resolution optical coherence tomography using a liquid crystal spatial light modulator," *Vision Res.* **45**, 3432–3444 (2005).
- Y. Zhang, J. T. Rha, R. S. Jonnal, and D. T. Miller, "Adaptive optics parallel spectral domain optical coherence tomography for imaging the living retina," *Opt. Express* **13**, 4792–4811 (2005).
- D. Merino, C. Dainty, A. Bradu, and A. G. Podoleanu, "Adaptive optics enhanced simultaneous *en-face* optical coherence tomography and scanning laser ophthalmoscopy," *Opt. Express* **14**, 3345–3353 (2006).
- A. E. Elsner, S. A. Burns, J. J. Weiter, and F. C. Delori, "Infrared imaging of sub-retinal structures in the human ocular fundus," *Vision Res.* **36**, 191–205 (1996).
- M. E. Hartnett and A. E. Elsner, "Characteristics of exudative age-related macular degeneration determined *in vivo* with confocal and indirect infrared imaging," *Ophthalmology* **103**, 58–71 (1996).
- C. Kunze, A. E. Elsner, E. Beausencourt, L. Moraes, M. E. Hartnett, and C. L. Trempe, "Spatial extent of pigment epithelial detachments in age-related macular degeneration," *Ophthalmology* **106**, 1830–1840 (1999).
- A. Remky, E. Beausencourt, M. E. Hartnett, C. L. Trempe, O. Arend, and A. E. Elsner, "Infrared imaging of cystoid macular edema," *Graefes Arch. Clin. Exp. Ophthalmol.* **237**, 897–901 (1999).
- M. Miura, A. E. Elsner, E. Beausencourt, C. Kunze, M. E. Hartnett, K. Lashkari, and C. L. Trempe, "Grading of infrared confocal scanning laser tomography and video displays of digitized color slides in exudative age-related macular degeneration," *Retina* **22**, 300–308 (2002).
- A. E. Elsner, Q. Zhou, F. Beck, P. E. Tornambe, S. A. Burns, J. J. Weiter, and A. W. Dreher, "Detecting AMD with multiply scattered light tomography," *Int. Ophthalmol.* **23**, 245–250 (2001).
- S. A. Burns, A. E. Elsner, M. B. Mellem-Kairala, and R. B. Simmons, "Improved contrast of subretinal structures using polarization analysis," *Invest. Ophthalmol. Visual Sci.* **44**, 4061–4068 (2003).
- C. R. Vogel, "Retinal motion estimation in adaptive optics scanning laser ophthalmoscopy," *Opt. Express* **14**, 487–497 (2006).
- R. H. Webb, "Confocal scanning laser ophthalmoscope," *J. Opt. Soc. Am. A* **3**, P52–P52 (1986).
- A. E. Elsner, S. A. Burns, R. Webb, and G. W. Hughes, "Reflectometry with a scanning laser ophthalmoscope," *Appl. Opt.* **31**, 3697–3710 (1992).
- A. Plesch and U. Klingbeil, "Optical characteristics of a scanning laser ophthalmoscope," in *Proc. SPIE* **1161**, 390–398 (1989).
- R. H. Webb, G. W. Hughes, and F. C. Delori, "Confocal scanning laser ophthalmoscope," *Appl. Opt.* **26**, 1492–1499 (1987).
- R. H. Webb, "Confocal optical microscopy," *Rep. Prog. Phys.* **59**, 427–471 (1996).
- K. Venkateswaran, A. Roorda, and F. Romero-Borja, "Theoretical modeling and evaluation of the axial resolution of the adaptive optics scanning laser ophthalmoscope," *J. Biomed. Opt.* **9**, 132–138 (2004).
- A. E. Elsner, L. Moraes, E. Beausencourt, A. Remky, S. A. Burns, J. J. Weiter, J. P. Walker, G. L. Wing, P. A. Raskauskas, and L. M. Kelley, "Scanning laser reflectometry of retinal and subretinal tissues," *Opt. Express* **6**, 243–250 (2000).
- D. X. Hammer, R. D. Ferguson, J. C. Magill, M. A. White, A. E. Elsner, and R. H. Webb, "Image stabilization for scanning laser ophthalmoscopy," *Opt. Express* **10**, 1542–1549 (2002).
- D. X. Hammer, R. D. Ferguson, J. C. Magill, M. A. White, A. E. Elsner, and R. H. Webb, "Compact scanning laser ophthalmoscope with high-speed retinal tracker," *Appl. Opt.* **42**, 4621–4632 (2003).
- D. X. Hammer, R. D. Ferguson, J. C. Magill, A. E. Elsner, and R. H. Webb, "Tracking scanning laser ophthalmoscope (TSLO): initial human subject testing," *Invest. Ophthalmol. Visual Sci.* **43** (Suppl.), U1260 (2002).
- J. S. McLellan, S. Marcos, and S. A. Burns, "Age-related changes in monochromatic wave aberrations of the human eye," *Invest. Ophthalmol. Visual Sci.* **42**, 1390–1395 (2001).
- D. T. Miller, L. N. Thibos, and X. Hong, "Requirements for segmented correctors for diffraction-limited performance in the human eye," *Opt. Express* **13**, 275–289 (2005).
- A. Tikhonov and V. Arsenin, *Solution of Ill-posed Problems* (Winston, 1977).
- P. M. Prieto, F. Vargas-Martin, S. Goelz, and P. Artal, "Analysis of the performance of the Hartmann–Shack sensor in the human eye," *J. Opt. Soc. Am. A* **17**, 1388–1398 (2000).
- A. V. Oppenheim, A. S. Willsky, and I. T. Young, *Signals and Systems*, Prentice-Hall Signal Processing Series (Prentice-Hall, 1983), p. 796.
- R. D. Ferguson, A. E. Elsner, R. H. Webb, and M. B. Frish,

- “Retinal tracking for SLO image stabilization,” *Invest. Ophthalmol. Visual Sci.* **41** (Suppl.), S167 (2000).
39. R. D. Ferguson, J. C. Magill, M. B. Frish, A. E. Elsner, and R. H. Webb, “The tracking SLO second generation retinal imaging performance,” *Invest. Ophthalmol. Visual Sci.* **42** (Suppl.), S4255 (2001).
40. R. D. Ferguson, D. X. Hammer, C. E. Bigelow, N. V. Iftimia, T. E. Ustun, S. A. Burns, A. E. Elsner, and D. R. Williams, “Tracking adaptive optics scanning laser ophthalmoscope,” *Proc. SPIE* **6138**, 232–240 (2006).
41. ANSI, “American National Standards for safe use of lasers,” in ANSI 136.1-1993 (revision of ANSI 136.1-1986) ANSI (1993).
42. F. C. Delori, R. H. Webb, and D. H. Sliney, “Maximum permissible exposures for ocular safety (ANSI 2000), with emphasis on ophthalmic devices,” *J. Opt. Soc. Am. A*, **24**, 1250–1265 (2007).
43. R. D. Ferguson, D. X. Hammer, and R. H. Webb, “A line-scanning laser ophthalmoscope (LSLO),” *Invest. Ophthalmol. Visual Sci.* **44** (Suppl.), U289 (2003).
44. A. E. Elsner, M. Miura, S. A. Burns, E. Beausencourt, C. Kunze, L. M. Kelley, J. P. Walker, G. L. Wing, P. A. Raskauskas, D. C. Fletcher, Q. Zhou, and A. W. Dreher, “Multiply scattered light tomography and confocal imaging: detecting neovascularization in age-related macular degeneration,” *Opt. Express* **7**, 95–106 (2000).
45. A. E. Elsner, A. Dreher, E. Beausencourt, S. Burns, Q. Zhou, and R. H. Webb, “Multiply scattered light tomography: vertical cavity surface emitting laser array used for imaging subretinal structures,” *Lasers Light Ophthalmol.* **8**, 193–202 (1998).
46. F. C. Delori, and K. P. Pflibsen, “Spectral reflectance of the human ocular fundus,” *Appl. Opt.* **28**, 1061–1077 (1989).
47. D. Van Norren and L. F. Tiemeijer, “Spectral reflectance of the human eye,” *Vision Res.* **26**, 313–320 (1986).
48. J. van der Kraats, T. T. J. M. Berendschot, and D. V. Norren, “The pathways of light measured in fundus reflectometry,” *Vision Res.* **15**, 2229–2247 (1996).
49. P. M. Prieto, J. S. McLellan, and S. A. Burns, “Investigating the light absorption in a single pass through the photoreceptor layer by means of the lipofuscin fluorescence,” *Vision Res.* **45**, 1957–1965 (2005).
50. S. S. Choi, N. Doble, J. Lin, J. Christou, and D. R. Williams, “Effect of wavelength on *in vivo* images of the human cone mosaic,” *J. Opt. Soc. Am. A* **22**, 2598–2605 (2005).
51. Y. Zhang, B. Cense, J. Rha, R. S. Jonnal, W. Gao, R. J. Zawadzki, J. S. Werner, S. Jones, S. Olivier, and D. T. Miller, “High-speed volumetric imaging of cone photoreceptors with adaptive optics spectral-domain optical coherence tomography,” *Opt. Express* **14**, 4380–4394 (2006).